Landslides (2022) 19:2423–2437
DOI 10.1007/s10346-022-01938-z
Received: 22 March 2022
Accepted: 8 July 2022
Published online: 2 August 2022
© The Author(s) 2022

Matthew E. Cook · Martin S. Brook · Ian J. Hamling · Murry Cave · Jon F. Tunnicliffe · Rachel Holley · David J. Alama

Engineering geomorphological and InSAR investigation of an urban landslide, Gisborne, New Zealand

Abstract The East Coast region of New Zealand has some of the highest erosion rates in the world, due to its proximity to an active plate boundary, susceptibility to high-intensity storms and steep terrain underlain by young soft sedimentary rock and soil. In the city of Gisborne, expansion of residential blocks into steeper terrain in peri-urban areas has required improved capacity for the characterisation and monitoring of slope stability. Landslides have affected several properties and have destroyed infrastructure. Slope failure commonly occurs during heavy rainfall events when slow-moving retrogressive slides transition into earthflows and mudflows. In this study, we used in situ sampling and testing methods combined with remote sensing techniques to provide an understanding of the pre-failure and post-failure behaviour of an urban landslide in Gisborne. High-resolution aerial imagery, unmanned aerial vehicle imagery and light detection and ranging data revealed slope morphology and contours of prehistoric failures in the area, and highlighted the more recent impacts of deforestation on slope stability. Furthermore, Sentinel-1 InSAR analysis determined that gradual deformation began in 2017, following two ex-tropical cyclone events. Deformation downslope continued until an initial failure in July 2020. Following that event, some parts of the slope proceeded to accelerate, leading to a further reactivation event in November 2021, following heavy rainfall. During this November 2021 event, average line of sight velocities ranged from −7.9 to −11.2 mm/year, and deformation rates in the vertical direction (related to rotational slumping) averaged −11.2 to −11.9 mm/year, consistent with field observations.

Keywords Urban landslide · New Zealand · Rainfall triggering · Remote sensing · InSAR

Introduction

Shallow landslides are among the most common types of landslides and are regularly triggered by high-intensity and long-duration rainfall events (Claessens et al. 2007; Galli et al. 2008; Minder et al. 2009). These types of failures are widespread throughout New Zealand's North Island, frequently occurring on steep terrain underlain by expansive soils and weak sedimentary rock (Basher 2013; Crozier 2010; Glade 2003; Phillips et al. 2018). The failure and transport of slope material by shallow landsliding is one of the principal soil erosion and slope development processes shaping New Zealand's landscape (Basher 2013; Claessens et al. 2007). New Zealand has one of the highest global erosion rates due to its temperate maritime, mid-latitude, active plate boundary setting and susceptibility to high-intensity storms (Phillips et al. 2018). Indeed, in Gisborne, a city on the east coast of the North Island (Fig. 1a) is where much of the worst erosion occurs. This is driven particularly by steep slopes, easily erodible material, high rainfall, extensive deforestation and large numbers of grazing animals (Basher 2013). While many of the landslides in the region occur on hillslopes in sparsely populated areas, many of these events impact productive land, affect infrastructure such as roads and bridges and damage or destroy residential properties (Davies and Cave 2017; Mazengarb 1997; Phillips et al. 2018; Rosser et al. 2017). Existing settlements may be unknowingly located on pre-historic landslide deposits, where landslide risk is largely unknown until a slope failure event occurs. In some cases, reactivation events affect the same properties multiple times. Nevertheless, there is continued residential development and urban expansion into suboptimal steep terrain, where the controls on hillslope stability are poorly understood. Hence, it is important to understand the processes and mechanisms of landslides that impact urban areas, particularly the relationship between environmental and anthropogenic factors. Indeed, landslide monitoring typically requires the continuous measurement of ground deformation, which is often done physically in the field using in situ techniques such as GPS/GNSS, inclinometer, extensometer or tiltmeter readings to extract deformation (Tang et al. 2014; Uhlemann et al. 2016). Although these techniques are highly effective, they monitor deformation at a low spatial and temporal resolution. Globally, over the past two decades, remote sensing techniques such as interferometric synthetic aperture radar (InSAR) have been used to map and monitor landslides and complement traditional on-site landslide observations and measurements (Aslan et al. 2020; Béjar-Pizarro et al. 2017; Colesanti and Wasowski 2006; Del Soldato et al. 2019; Isya et al. 2019; Notti et al. 2014), particularly since the launch of Sentinel-1 in 2014. This was the first civilian satellite designed explicitly for InSAR analysis and producing free, open-access data (Ferretti et al. 2015).

In this paper, we use field reconnaissance, remote sensing and preliminary laboratory work to investigate a shallow landslide above Richardson Avenue in Gisborne city, New Zealand (Fig. 1b). The initial failure occurred on July 20, 2020, and was characterised by rotational slumping at the headscarp, transitioning downslope into a channelised mudflow. Heavy rainfall on November 4, 2021, subsequently triggered a minor reactivation event. A combination of methods was used to gather data on the landslide pre- and post-failure, including in situ soil sampling and testing, unmanned aerial vehicle (UAV) imagery, ground penetrating radar (GPR), light detection and ranging (LiDAR) and InSAR. These approaches, along with site details, are outlined below. The InSAR revealed that the slope had been actively deforming since 2017 and continued to show movement

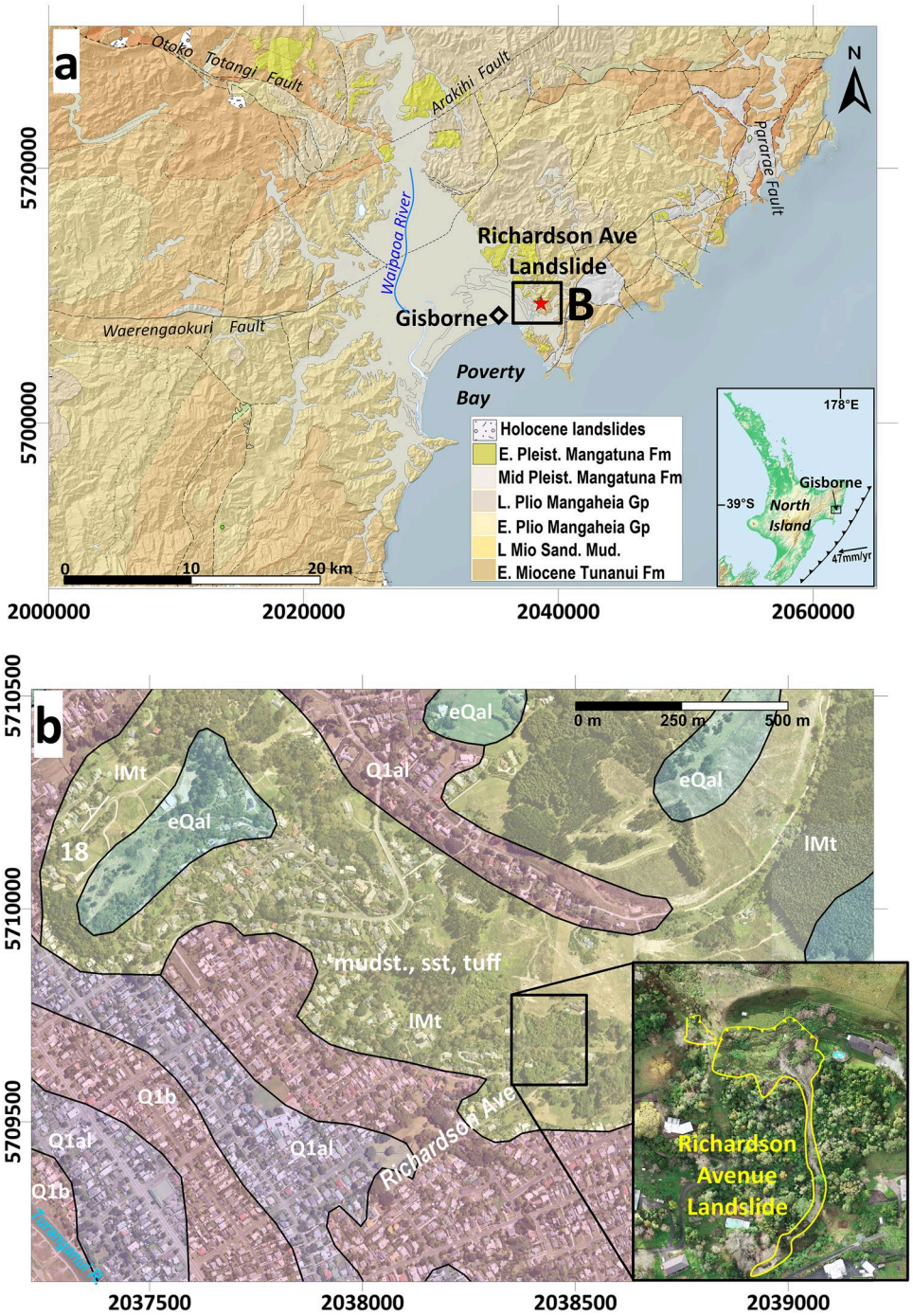


Fig. 1 **a** Location of Gisborne on the North Island and major structures of the convergent Hikurangi margin and the regional geology and geomorphology of the area surrounding Gisborne City; **b** map of the main lithologies in the study area, and the extent and geomorphology of the July 2020 Richardson landslide

after the initial failure, prior to the reactivation event. Thus, in the future, InSAR, along with UAV imagery and in situ techniques, should be helpful for detecting, mapping and monitoring landslides in the urban area and assist with planning and decision-making.

Study area

Gisborne city is located on the Raukumara Peninsula on the east coast of New Zealand's North Island (Fig. 1). The city contains 60% of the entire region's buildings (Grace 2014) and is primarily built upon the Poverty Bay Flats, a low-lying alluvial flood plain of the Waipaoa River. Surrounding the plain are steep hills composed of Neogene and Quaternary weak sedimentary rocks and soils (Fig. 1). Many of these hillslopes are exposed to overgrazing and deforestation, and their stability is often compromised by slope modifications such as dirt tracks and unregulated construction. The Richardson Avenue landslide is located on a south-facing slope below one of the more prominent and steep ridgelines in the city, in the suburb of Whataupoko. Steep surfaces on the south-facing slope range between 25° and 47° and 35° to 50° on the north-facing slope. The morphology of the slope pre-failure is shown in Fig. 2a

using a hillshade raster overlain by a digital elevation model (DEM) from a 2019 LiDAR survey. The landslide occupies three different land parcels, commencing just below the ridgeline north of 35 Richardson Avenue, and terminating 150 m downslope near 16 Adams Road, where sediment runout was deposited in 2020 (Fig. 2a). Ridges constrain the landslide on either side and indicate the slope is part of a larger paleo-headscarp (Fig. 2), representing a larger pre-historic slope failure. The DEM in Fig. 2a illustrates the "stepped" morphology of the slope, partly influenced by anthropogenic modifications such as the dirt track below the headscarp and the ridgeline on the western side of the landslide (Fig. 2a). The geology in the study area is late Miocene Tolaga Group mudstone (lMt), with minor sandstone and tuff (Fig. 1), and no faults have been mapped in the area. There is an outcrop of the Quaternary Mangatuna Formation on the adjacent hilltop, composed of fossiliferous clay, tephra, sandstone and blue-grey mudstone (Fig. 1). This

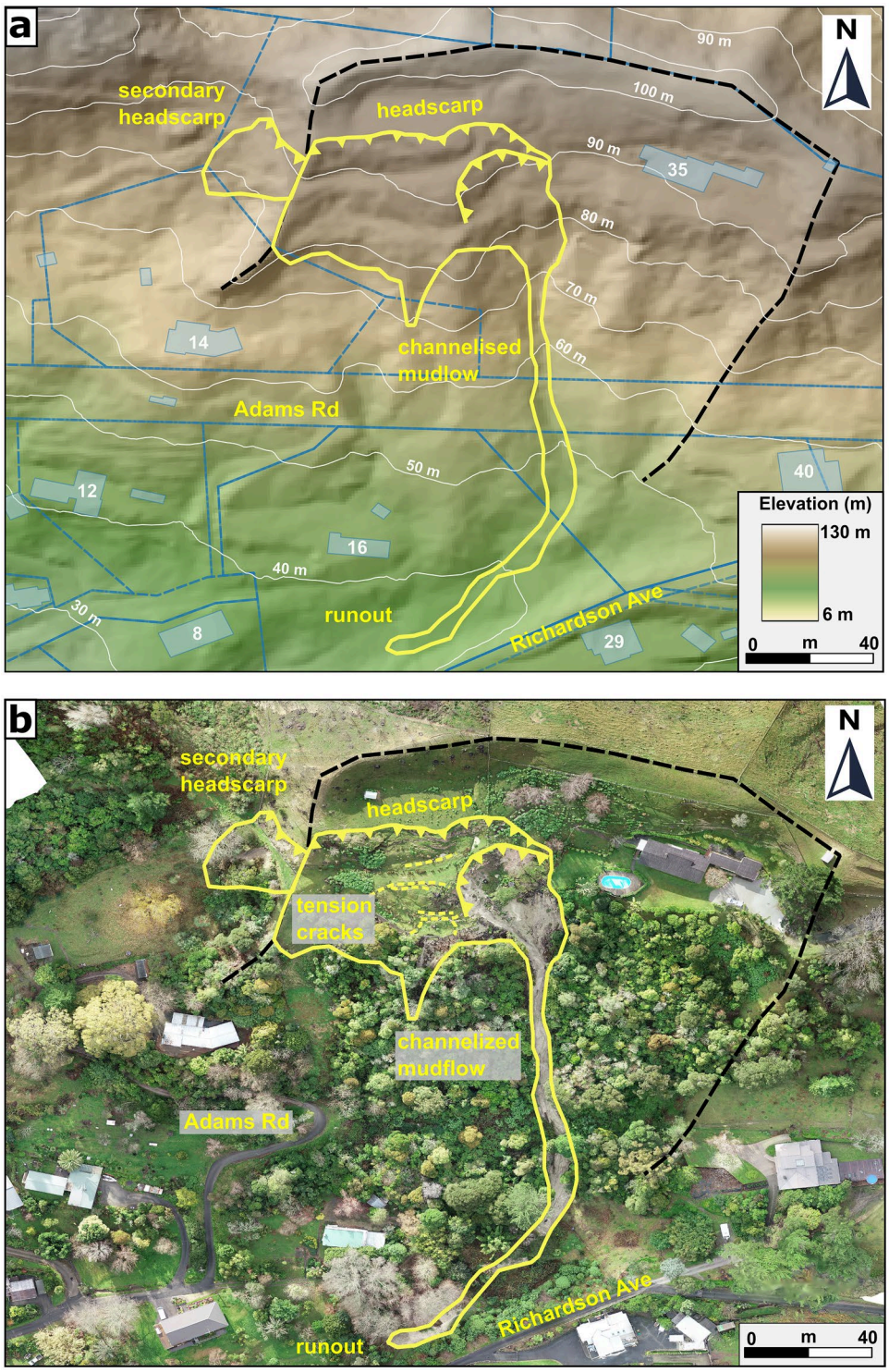


Fig. 2 **a** Map of the Richardson landslide overlain on the 2019 LiDAR DEM with the extent of the 2020 landslide outlined and property and building tiles; **b** UAV image of the landslide. The upper section of the landslide is dominated by rotational slumping, which transitions into a narrow, channelised mudflow

unit is commonly found on top of ridgelines across the city and is associated with shallow soil failures (Mazengarb 1997).

Methods

Geomorphological data collection

A timeline of surface geomorphic evolution at the study area was obtained using high-resolution aerial imagery from 2012 and 2017 and historical imagery from Retrolens (retrolens.nz) (Fig. 3). In addition, a UAV survey was undertaken after the July 2020 failure, which provided georeferenced images of the whole site to aid geomorphological interpretation. A LiDAR survey undertaken in January 2019 was also used to identify geomorphic features of the slope before the failure occurred.

Material properties

Field surveys were undertaken after the complete failure of the slope in July 2020 and were used to augment the geomorphological mapping. Soil samples for in situ testing and laboratory analysis were obtained from three auger hole locations on the landslide (Fig. 4a). Field descriptions followed the New Zealand Geotechnical Society Guidelines (NZGS) outlined in Burns et al. (2005). A Geotechnics hand-held shear vane tester was used to obtain field estimates of shear strength (undisturbed, S_u; disturbed, S_d) and compressive strength, respectively. A Scala dynamic cone penetrometer (Chaney et al. 2001) was used to evaluate the strength of the subsurface. The method involves using a 9-kg weight dropped from a height of 510 mm to drive a 60° cone into the ground. The number of blows required to drive the cone 100 mm were recorded until refusal (>17 blows). In situ samples were taken for moisture content and dry bulk density analysis, and samples were oven-dried overnight to 105 °C. Then, the dried samples were crushed and sub-sampled for particle-size distribution analysis using a Malvern Mastersizer 2000. Atterberg limits were obtained on the < 0.425-µm size fraction of samples following the procedures outlined in BS 1377–2 (BSI 1998). The soil dispersion potential was investigated using the Emerson class number, following AS 1289.3.8.1 (2006). In addition, an FEI Quanta 200 field emission scanning electron microscopy (SEM) was used to confirm the presence of clay minerals.

Ground penetrating radar

Ground penetrating radar (GPR) is a common technique for investigating subsurface structure and stratigraphy. This is based

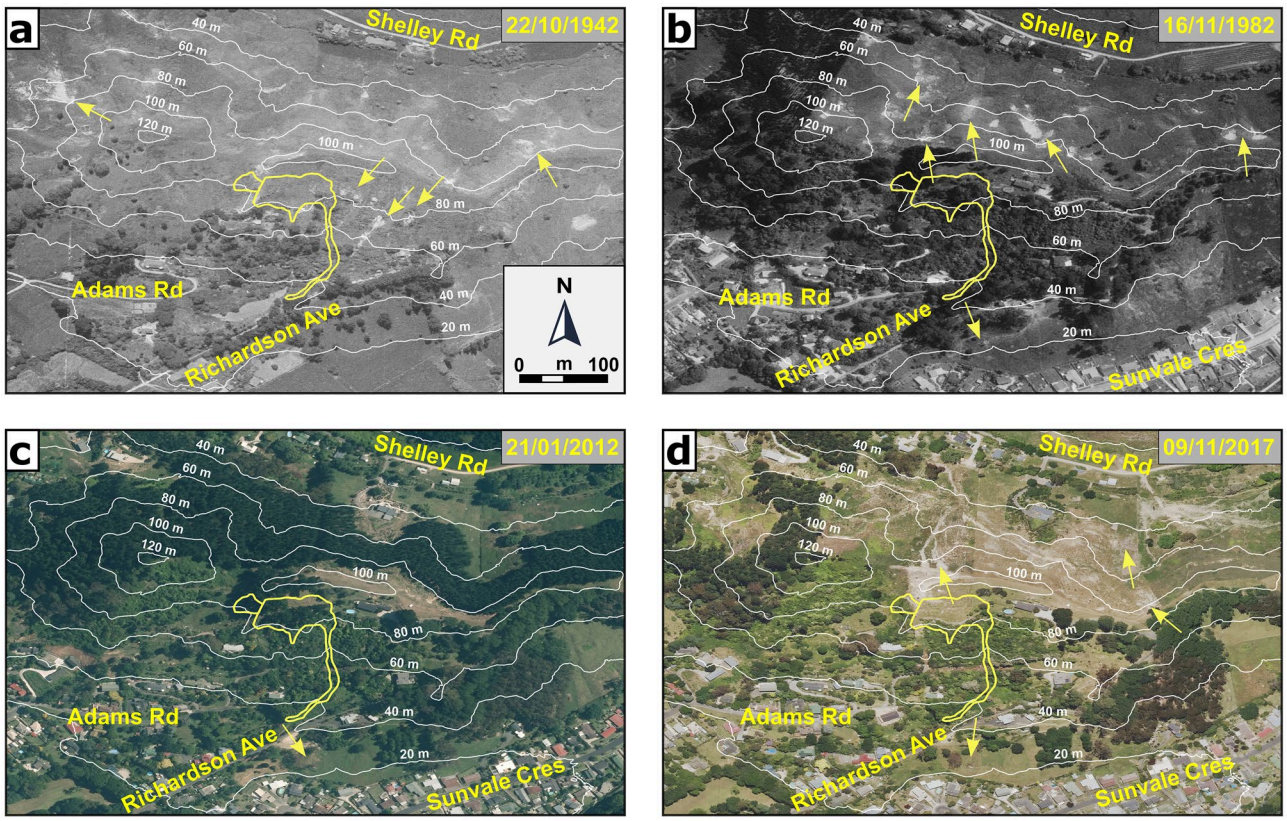


Fig. 3 Historical aerial images with the July 2020 landslide extent outlined in yellow. Yellow arrows indicate shallow soil failures on slopes; **a** 1942 image showing shallow soil failures on the south-facing slopes in the gully adjacent to the current failure; **b** 1982 image showing extensive failures on the north-facing slopes and southern slopes stabilised by vegetation; **c** thick vegetation on the north and south-facing slopes, showing relative stability; **d** pine trees cut down from on top of the ridge and where current the headscarp is located. Evidence of shallow soil failures on the north facing slope

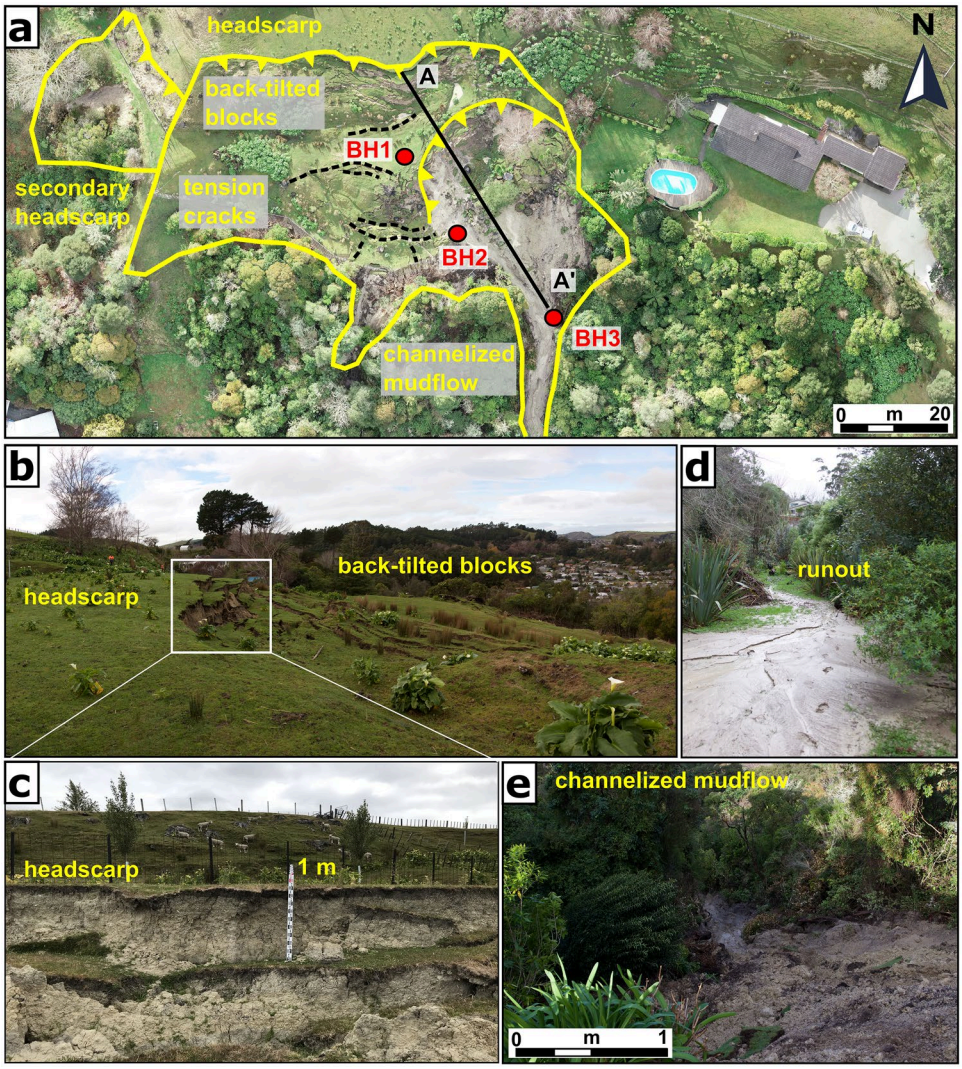


Fig. 4 **a** Map showing the locations of hand-auger boreholes and GPR transect; **b** headscarp area that has been deforested and slumping has caused back tilted blocks; **c** headscarp; **d** mudflow runout; **e** the transition between the zone of rotational slumping and channelised mudflow

on the principle of transmission of an electromagnetic signal into the subsurface, with the portion of that signal being reflected back to the surface related to the variable dielectric properties of the materials (Jol 2008). GPR imaging of the near-subsurface was conducted using a 160-MHz Mala GX HDR shielded antenna (fixed spacing of 0.33 m) mounted on an all-terrain cart, with integral GPS. The transect extended southward along the midpoint of the slope failure (Fig. 4), with the aim of intersecting the three boreholes as closely as possible (although the lateral offset from BH1 and BH 2 was ~ 9 m). The horizontal sampling interval was 0.049 m, along the 53-m-long transect. Processing of the GPR data was completed using RadExplorer 1.4.2 and standard processing routines were applied including desaturation, first arrival time correction, amplitude correction, bandpass filtering and migration (e.g. Jol 2008). The GPR data was topographically corrected based on the site elevation model. A simple depth-averaged radar wave velocity structure was assumed of 0.1 m/ns, based on typical published velocities for dry, clayey soils (e.g. Jol 2008).

InSAR data and processing

We applied the small baseline subset technique (Berardino et al. 2002) to identify landslide-related deformation within the study area. Sentinel-1 images from 2016 to 2021 with a revisit time of 12 days between each image were used from descending and ascending orbit directions. From the descending track 175, 137 acquisitions were used to generate a stack of 405 interferograms and 153 images were used from the ascending track 8 to generate a stack of 453 interferograms. We used three connections per image for our network to reduce the temporal decorrelation. The stacks of SAR images were processed using ISCE (Rosen et al. 2012), and displacement and time series were obtained using MintPY (Yunjun et al. 2019). All measurements were taken with respect to a stable reference point that was assumed to be nondeforming (−38.655°S, 178.039°E). As the landslide geometry is perpendicular to the line of sight (LOS) of the satellites, the sensors are not as sensitive to north–south slope movement as they would be for an east–west-oriented slope. Thus, determining slope deformation is more

challenging. However, with datasets from two different viewing geometries, the vertical and horizontal (E-W) movement can be obtained (Notti et al. 2014) by combining the LOS vectors (E, U) and the velocity in the direction of LOS (V_{LOS}) for the ascending (V_{asc}) and descending (V_{desc}) datasets, using the following formula:

$$V_{EW} = \frac{\left(\left(\frac{V_{desc}}{U_{desc}}\right) - \left(\frac{V_{asc}}{U_{asc}}\right)\right)}{\left(\left(\frac{E_{desc}}{U_{desc}}\right) - \left(\frac{E_{asc}}{U_{asc}}\right)\right)} \quad (1)$$

$$V_{VERT} = \frac{\left(\left(\frac{V_{desc}}{E_{desc}}\right) - \left(\frac{V_{asc}}{E_{asc}}\right)\right)}{\left(\left(\frac{U_{desc}}{E_{desc}}\right) - \left(\frac{U_{asc}}{E_{asc}}\right)\right)} \quad (2)$$

where the LOS vectors are a component of the incidence angle (α) and heading angle (γ), in radians (Notti et al. 2014):

$$E = -1 \cdot \sin(\alpha) \cdot \sin(\gamma) - \frac{3 \cdot \pi}{2} \quad (3)$$

$$N = -1 \cdot \sin(\alpha) \cdot \cos(\gamma) - \frac{3 \cdot \pi}{2} \quad (4)$$

$$U = \cos(\alpha) \quad (5)$$

The V_{VERT} is used to highlight the impact of the vertical displacements related to the rotational component of the landslide, because the sensors will have low sensitivity to any southward, horizontal or translational displacements (V_{EW}) along the south-facing slope (Notti et al. 2014).

Results

Geomorphic change

A sequence of available historic aerial images (Fig. 3) shows that the area has been subject to periodic instability and slope failure activity on both the north-facing and south-facing slopes. Periods of activity coincide with recent forest clearance. A shallow failure can be seen on the south-facing slope in Fig. 3a (1942), coinciding with the current location of the house at 35 Richardson Avenue. By 1982, the south-facing slope had regrown a cover of dense vegetation and showed no signs of further activity, but several shallow failure events occurred on the steep north-facing slope (Fig. 3b). In 2012, both slopes were covered in thick pine trees (Monterey Pine; *Pinus radiata*) and appeared stable (Fig. 3c). Then, in 2015, pine trees were stripped from the slopes as they were deemed a hazard to properties below, and the location of the current headscarp became exposed (Fig. 3d). Extensive rainfall occurred through April–July 2017, and exposed sediment can be seen on the north-facing slope, but no significant failure was recorded (Fig. 3d). Complete failure of the south-facing slope occurred in the early morning on the July 20 2020, following 7 days of continuous rainfall (total = 88 mm). The morphology of the July 2020 failure is superimposed on the UAV image in Fig. 2b, and site photos are shown in Fig. 4. The failure is a "complex" (e.g. Hungr et al. 2014), primarily composed of rotational slumping, tension cracks and back-tilted blocks (Fig. 4a) at the top of the slope, which transitions into a channelised mudflow within a narrow gully (Fig. 4d) that extends ~ 160 m downslope (Fig. 4e). A secondary headscarp also appeared on the western side of the ridge, with slight movement occurring above and below a farm access track (Fig. 4a). The current headscarp region is below the ridgeline 75 m west of the house at 35 Richardson Avenue and has subsided ~ 1 m in places (Fig. 4b, c). An unusual, slow-moving tropical storm crossed Gisborne on 4 November 2021, causing 250.7 mm of rainfall over 5 days. This one in 50-year event caused a minor reactivation of the Richardson Avenue landslide 25 m below the 2020 headscarp (Fig. 5). The small rotational slump regressed 5 m from its July 2020 position, towards an area where large tension cracks were present (Figs. 4a and 5).

Subsurface properties and structure

Field descriptions of the soils are presented in Table 1 and a summary of the soil properties taken at the three hand auger holes on the landslide is reported in Table 2. The locations of the sample sites are shown in Fig. 4 a. Particle-size distribution was determined for these samples (Table 1) and is displayed in Fig. 6. The percentage of fine particle size (< 60 μm) exceeds 35% for all samples, so the soils are classed as cohesive. Based on the NZGS 2005 guidelines (Burns et al. 2005), almost all samples are classified as clayey SILT with some/minor sand, with one sample classed as silty CLAY with minor sand (Table 1). Indeed, the distribution curve shows that the soils are dominated by (45–67%) silt-sized gradings, as well as clays (10–50%), but all samples also contain fragments of sand particles (5–30%). Table 2 shows that all the samples have an in situ moisture content (w) lower than the liquid limit (w_L), but higher than the plastic limit (w_P), indicating the soils are in a plastic state, except for the sample retrieved at BH2 1.5 m, where water was encountered. That soil was saturated and acted like a slurry. The relationship between the liquid limit and plasticity index (I_P) is shown on the plasticity chart (Fig. 6). All samples were identified as clays with medium to high plasticity. Two samples from BH1 were classified as fat clays (CH) exhibiting high plasticity, while the rest of the samples were lean clays displaying medium plasticity (Fig. 6). The samples' liquidity index (I_L) ranges between 0.5 and 1.3, suggesting that most of the soils will behave in a semi-plastic state (0–1). However, the sample at BH2 has an I_L of 1.3 and is in a liquid state. The soil undrained shear strength (S_u) at BH1 (Table 2) is firm (25–50 kPa) to stiff (50–100 kPa), while the soils at BH2 and BH3 are stiff to very stiff (100–200 kPa). The sensitivity index (SI) values of the soils range from 2.5 (moderately sensitive) to 16.9 (quick), with most of the samples classified as moderate (2–4) to sensitive (4–8), following Skempton and Northey (1952). The only sample classed as quick was BH2 1.5 m, and the high sensitivity value is due to the high water content of the soil at this depth. The activity chart shown in Fig. 6 was plotted following Skempton and Northey (1952), and the values range between inactive (< 0.75) and active (> 1.25) clays. The two fat clays from BH1, which have higher plasticity than the other samples, are classed as inactive clays, while the bulk of the samples plot as normal clays (0.75–1.25). The soil dispersion potential, as measured using the Emerson class number, is 1–2 for all the samples (Table 2), which implies the soils are moderate to highly dispersive. Imaging of samples under SEM (Fig. 6) confirmed the presence of clay minerals and gave insight into the clay minerals' microstructure. Identifiable features such as preferential alignment are present and share a similar structure to the smectite-rich soils reported at the Wallis

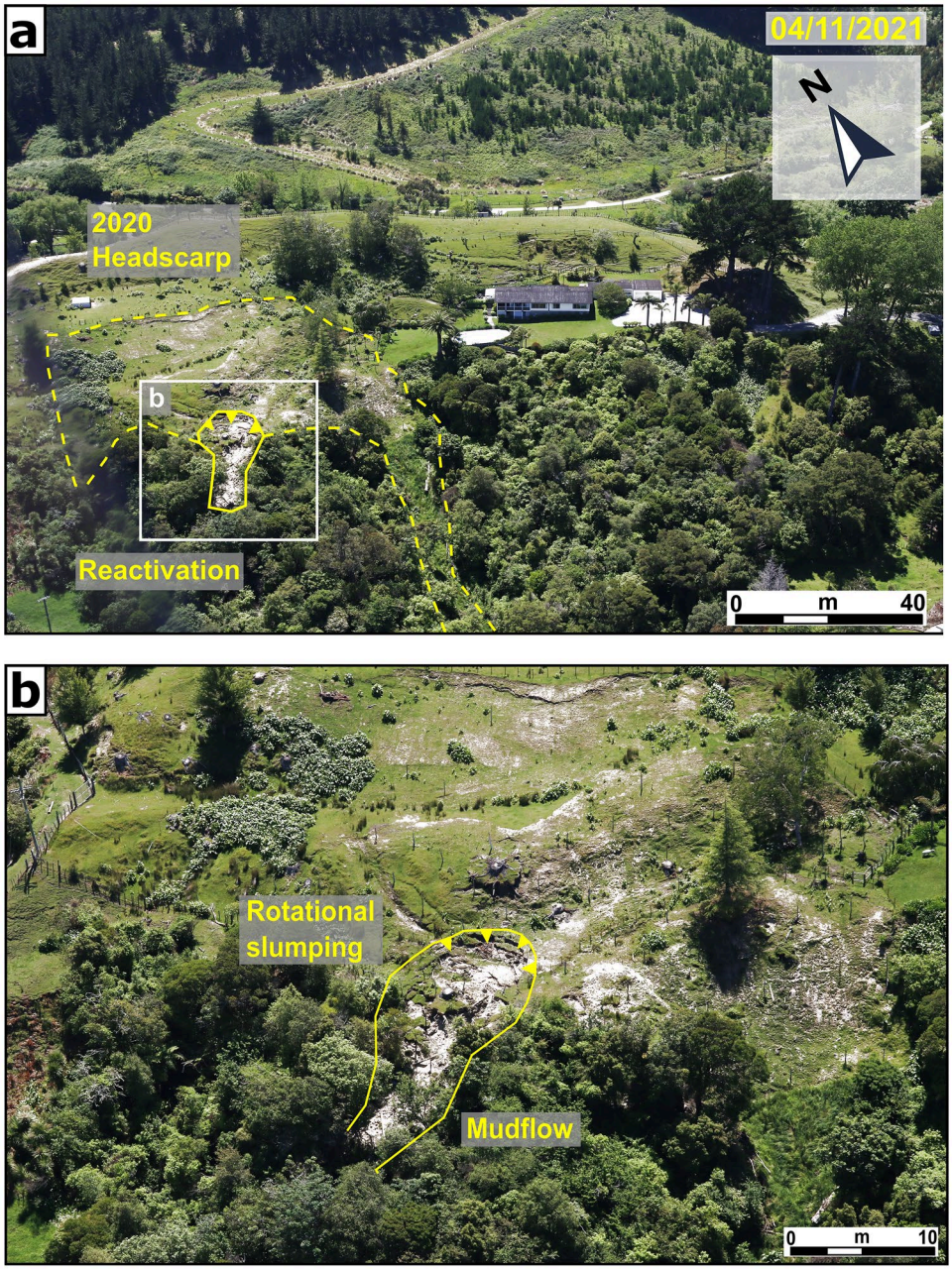


Fig. 5 **a** Geomorphological map showing the reactivation of the slope on the 4th of November 2021. The dashed yellow line represents the outline of the July 2020 failure. The white box highlights the reactivation event; **b** a minor reactivation on one of the secondary headscarps showing rotational slumping that becomes mobilised into a mudflow downslope

Road landslide in Gisborne (e.g. Cook et al. 2022). Indeed, smectite clay minerals are characterised by having very small particles, even among the clay minerals, and well-developed sheet-like structures (Fityus and Buzzi 2009; Meunier 2006).

To augment the interpretation of the borehole data and soil sampling and testing, the GPR profile (Fig. 4a for location) down the centre of the landslide is shown in Fig. 7. Surface observations coupled with boreholes revealed that subsurface structures and lithofacies correspond with the GPR data. The radargram broadly indicates a zone of tension and slumping in the upper part of the profile, a transition zone, terminating in a prograding lobe of channelised mudflow material, downslope (Fig. 7). Indeed, the strong, laterally continuous reflectors represent soil layers with contrasting dielectric properties to ~ 2-m depth. Below ~ 2-m depth, reflections become weaker, coinciding with a transition into stiffer soils, as shown by the penetrometer data (Fig. 7). At the upper-most end of the GPR profile, the typical pattern of strong continuous reflectors that are apparent in the subsurface further downslope is disturbed. Indeed, in some places of the upper part of the GPR radargram, reflectors are discontinuous, and these areas coincide with tension cracks and scarplets on the land surface caused by rotational slumping and back-tilting of blocks (e.g. Fig. 4). Towards the lower end of the profile (chainage 40–55 m), between 2- and 4 m depth, strong reflections are rare in the subsurface, but high amplitude reflectors appear below this low amplitude zone, at 4–6 m depth. This deeper series of reflectors is interpreted as accreted layers of a succession of channelised

Table 1 Soil descriptions and constituents encountered at the auger holes. Soil descriptions and terminology is based on the NZGS 2005 soil guidelines (Burns et al. 2005)

Site	Depth	Clay (%)	Silt (%)	Sand (%)	NZGS 2005 field description
BH1	0.5	47	58	5	Clayey SILT with minor sand, grey brown. Dry, firm. Rootlets present
	1.5	50	45	5	Silty CLAY with minor sand, light grey. Moist, low plasticity
	2.0	31	47	22	Clayey sandy SILT, grey brown. High plasticity
BH2	0.0	21	67	12	Clayey SILT with some sand, grey brown. Moist, high plasticity. Rootlets present
	1.5	21	59	20	Clayey SILT with some sand, grey brown. Saturated
BH3	0.0	10	60	30	Sandy SILT with minor clay, dark brown. Low plasticity. Rootlets present
	0.5	21	57	22	Clayey sandy SILT, grey brown. Hard, high plasticity. Iron staining
	1.0	25	65	10	Clayey SILT with some sand, blue grey. Hard, iron staining
	1.5	28	67	5	Clayey SILT with some sand, blue grey. Dry, hard. Iron staining

mudflow and earthflow events that terminate at the same general mid-slope position, forming a lobe. The dynamic cone penetrometer varied for each auger hole, but the general trend showed an increase in blows with depth (Fig. 7). At BH1, the blows range from 1 to 5, classed as "very loose" to "medium dense" in the NZGS (Burns et al. 2005) density index, until 2.2 m, where the blows increase to 11 and 20 (dense to very dense). For BH2, the soil density ranges from loose to medium dense, except at 1 m and 1.5 m, where the soil is very loose (Fig. 7), and water was observed. The soil becomes dense to very dense below 1.7 m. At BH3, located at the base of the rotational slumping before the transition into the channelised mudflow, the soil is very loose until 1 m bgl, and then the hard blue-grey clayey SILT is encountered, and the soil gradually becomes stiffer (Fig. 7).

InSAR analysis

The results of the InSAR analysis for the descending and ascending data sets are presented in Figs. 8 and 9, respectively. The velocity (mm/year) is measured in the direction of LOS (V_{LOS}), which is westward for descending and eastward for ascending. Negative values indicate movement away from the sensor, while positive values indicate movement towards the sensor. Both ascending and descending results show points with average velocities moving away from the sensor within the landslide polygon. The descending data set has several points clustered in the NE corner of the landslide surrounding the headscarp, with an average V_{LOS} of −7 to −11 mm/year (Fig. 8a). The ascending data set has more points within the landslide polygon, and the average V_{LOS} range from −4 to −16 mm/year. In order to compare the data sets, two points were selected from inside the landslide polygon (deforming) and two from outside (stable) for each data set (Figs. 8 and 9). The points selected inside the landslide were chosen close to the headscarp (Figs. 8a and 9a). Both ascending and descending results show that the points within the landslide polygon have similar deformation trajectories over time, suggesting a similar underlying deformation signal, and have been moving away from the satellite sensor since 2017 (Figs. 8b and 9b). A change in the downward trend is observed in both datasets slightly before the 20 July 2020 failure, as deformation moves towards the satellite (Figs. 8b and 9b). Although D1

Table 2 Soil index and geotechnical properties of selected hand auger samples

Site	Depth	S_u (kPa)	S_d (kPa)	SI	w (%)	w_L (%)	w_P (%)	I_P (%)	I_L (%)	Clay (%)	Silt (%)	Sand (%)	ECN
BH1	0.5	34	12	2.8	35.5	46	26.7	19.3	0.5	47	58	5	2
	1.5	81	19	4.3	39.1	64	28.1	35.9	0.3	50	45	5	1
	2.0	90	22	4.1	51.4	58	28.9	29.1	0.8	31	47	22	1
BH2	0.0	106	19	5.6	26.7	36.5	21.4	15.1	0.3	21	67	12	2
	1.5	203	12	16.9	52.2	46	24.4	21.6	1.3	21	59	20	2
BH3	0.0	140	25	5.6	32.4	32.4	19.6	12.8	1	10	60	30	2
	0.5	62	19	3.3	30.8	40	20.7	19.3	0.5	21	57	22	2
	1.0	153	62	2.5	22.1	38.9	19.9	19	0.1	25	65	10	2
	1.5	206	34	6.1	23.0	41.9	19.5	22.5	0.2	28	67	5	2

S_u undisturbed shear vane, S_d disturbed shear vane, SI sensitivity index, w in situ moisture content, w_L liquid limit, w_P plastic limit, I_P Plasticity Index, I_L Liquidity Index, *ECN* Emerson class number

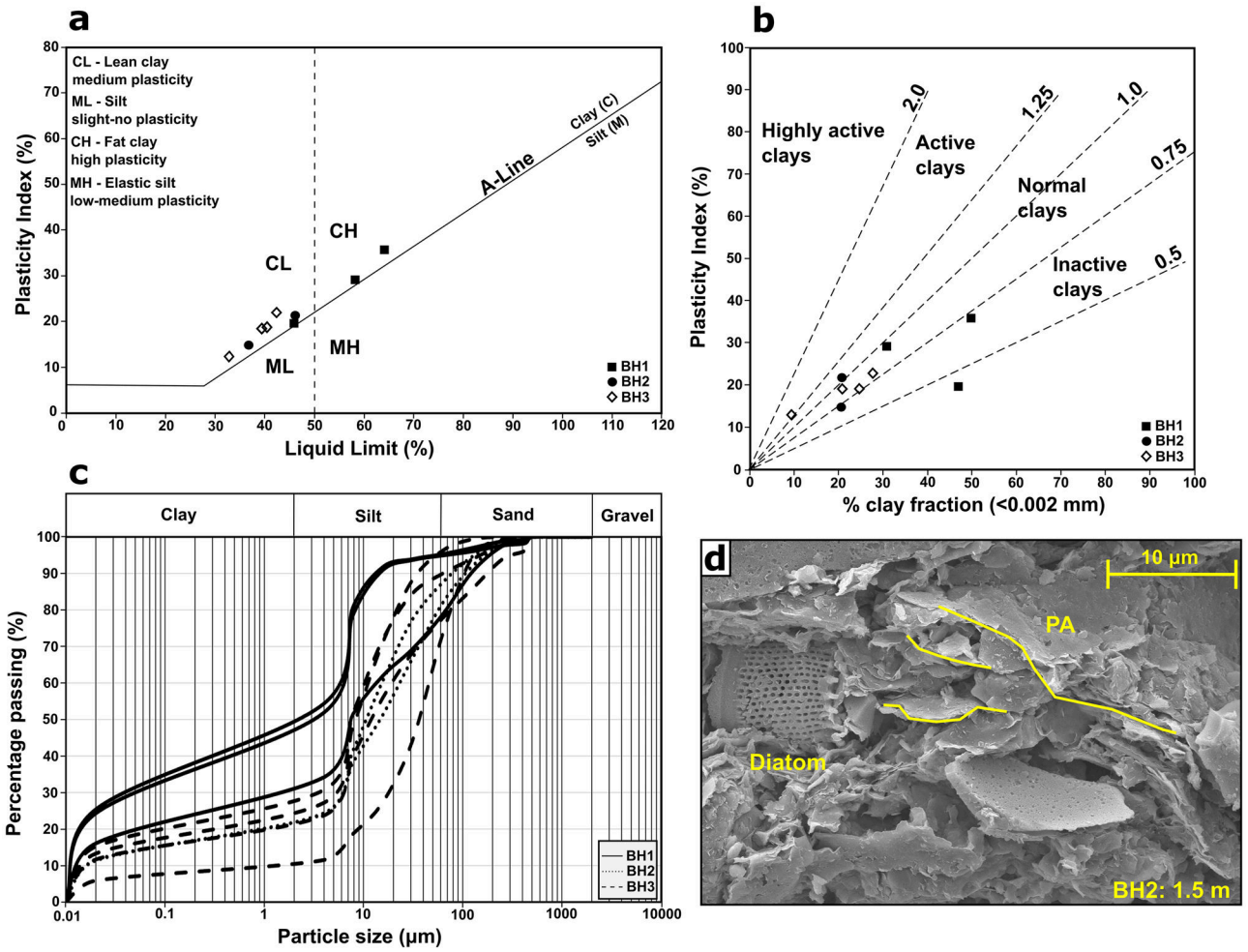


Fig. 6 Material properties of soil samples taken from BH1, BH2 and BH3; **a** plasticity chart; **b** activity chart; **c** PSD curve; **d** SEM image showing preferential alignment of particles (PA) and a diatom

and D2 have a similar downward trend, D2 shows more deformation (−74 mm) than D1 (−51 mm; Fig. 8b). The same correlation is seen with A1 and A2, with A2 lowering −54.45 mm and A1 −41 mm (Fig. 9b). In fact, D2 and A2, which are both below the main headscarp, exhibit acceleration after the 2020 failure. In contrast, D1 and A1, which are on or above the headscarp, are more stable after the failure in 2020 (Figs. 8b and 9b). These results indicate spatial differences in the rate of measured displacement and suggest that a zone of deformation within the lower slope continued to evolve leading up to the November 2021 reactivation event. This is consistent with the on-site observations (Fig. 5). In contrast, the "stable" points show little coherent change and are consistently between 5 and −5 mm for both ascending and descending data sets (Figs. 8b and 9b). Other areas with subsiding V_{LOS} values are seen on the north-facing slope and on the small south-facing slope above Sunvale Crescent (Figs. 8 and 9). The deformation detected is also related to slow shallow soil movements on exposed slopes, as observed in Fig. 3, although complete failure did not occur on these slopes.

In order to determine the actual slope displacement, the vertical (V_{VERT}) and east–west horizontal (V_{EW}) components were obtained at the headscarp using the LOS vectors and the V_{LOS} for D1 and A1 and D2 and A1. The results are displayed in Table 3 and show that at the headscarp, there was −11.2 to −11.9 mm/year of deformation in the vertical direction and −1.5 to −2.3 mm/year in the east–west direction. The results indicate that much of the motion detected was in the vertical direction and a small amount in the horizontal, which is consistent with a predominantly rotational component near the headscarp area.

Discussion

Material properties

The soils analysed from the landslide are fine-grained cohesive soils with high percentages of clay and silt, and have a medium to high plasticity. The high in situ moisture content, sensitivity and activity of the soils indicate the presence of swelling clays, which are often found in weathered residual soils (Asuri and Keshavamurthy 2016; Wesley 2010). Previous work on soils in Gisborne (e.g. Cook et al. 2022) reported smectite was the most common clay mineral, followed by illite on soil-mantled slopes within the Mangatuna Formation and Tolaga Group. Expanding clay minerals would induce

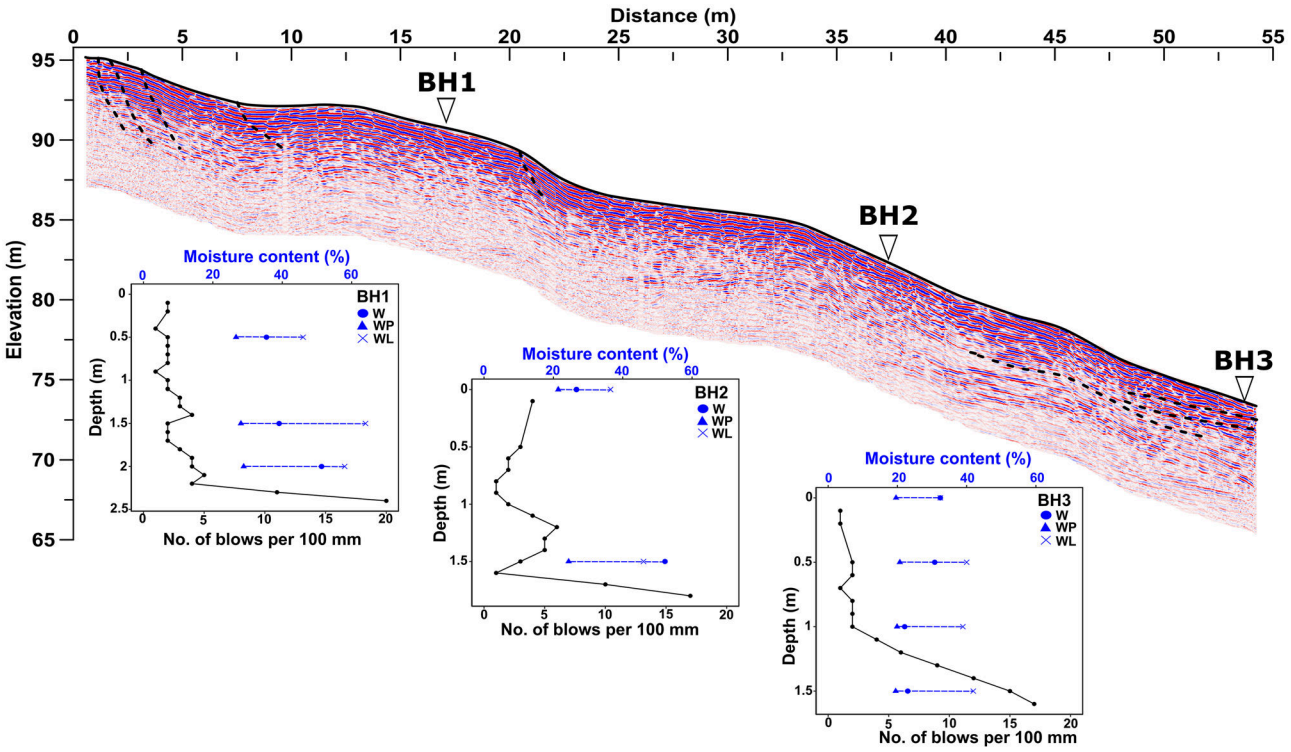


Fig.7 GPR transect down the centre of the landslide (Fig. 4a line A-A'), showing the location of the hand auger holes. Dashed black lines indicate key subsurface features such as tension cracks, back-tilted blocks and the breaks in reflectors suggest changes in the stratigraphy with depth near the toe. The plots highlight the *w*, in situ moisture content; w_L, liquid limit; w_P, plastic limit and results from the DCP for each auger hole

shrinkage and cracking of the soils during dry periods, and swelling during wetter periods (Wesley 2010).

The soil at BH2 is a good representation of how soils on the landslide behave once saturated, with high sensitivity (quick clay) and loss of strength upon remoulding, causing high mobility and runout potential. Torrance (2014) describes quick clays as fine-grained soils with high sensitivity and low activity clay-sized particles, such as the smectite-rich and high sensitivity clays of Scandinavia, North America and Canada, which have very low activities (0–0.1). At Richardson Avenue, activities of expanding soils were observed in the range of 0.4–1.25. The location of BH2 is adjacent to the tension cracks that formed after the 2020 failure (Fig. 4a), where the 2021 reactivated scarp is located (Fig. 5). Tension cracks would have provided a pathway for water to percolate down and saturate the soil, increasing the pore water pressure, reducing the shear strength, increasing the void ratio of the soil (Kim et al. 2004), increasing its mobility.

Furthermore, rotational slip surfaces are common in cohesive fine-grained soils, particularly where slopes are over-steepened or undercut by excavation (Hearn et al. 2011). The weathered blue-grey clayey SILT layer found at the base of BH3 provides a possible shear surface, allowing sliding and rotation. A contrast in permeability between weathered clayey SILT and an impermeable Tolaga Group mudstone layer below would increase the pore water pressure in the overlying soils. However, a more detailed ground investigation and modelling are required to more clearly delineate the shear surface(s) depth and extent (Hearn et al. 2011).

InSAR

Although InSAR has proven to be a valuable approach for remote sensing of landslide deformation (Aslan et al. 2020; Béjar-Pizarro et al. 2017; Bekaert et al. 2020; Colesanti and Wasowski 2006; Del Soldato et al. 2019; Handwerger et al. 2019; Intrieri et al. 2017; Isya et al. 2019; Notti et al. 2014), there are limitations regarding discernment of deformation process mechanics. Delineating process mechanisms of failure from InSAR is usually dependent on slope conditions, geometry and sensor used (Colesanti and Wasowski 2006). InSAR is primarily suitable for measuring slow deformation, because excessively rapid movement between acquisition dates will create phase ambiguity or a loss of coherence (e.g. Ferretti et al. 2015; Notti et al. 2014). Thus, the focus of InSAR in this study is on monitoring processes moving at very slow (16 to < 1.6 m/year) to extremely slow (< 16 mm/year) velocities (as defined by Hungr et al. 2014), rather than detecting maximum velocity at failure. The InSAR applications used in this investigation is limited by the number of coherent points in the landslide polygon, which is due to the spatial resolution of Sentinel-1 (approximately 5 m in E-W and 20 m in N-S) compared to the relatively small size of the target area (Wasowski and Bovenga 2014). Furthermore, the

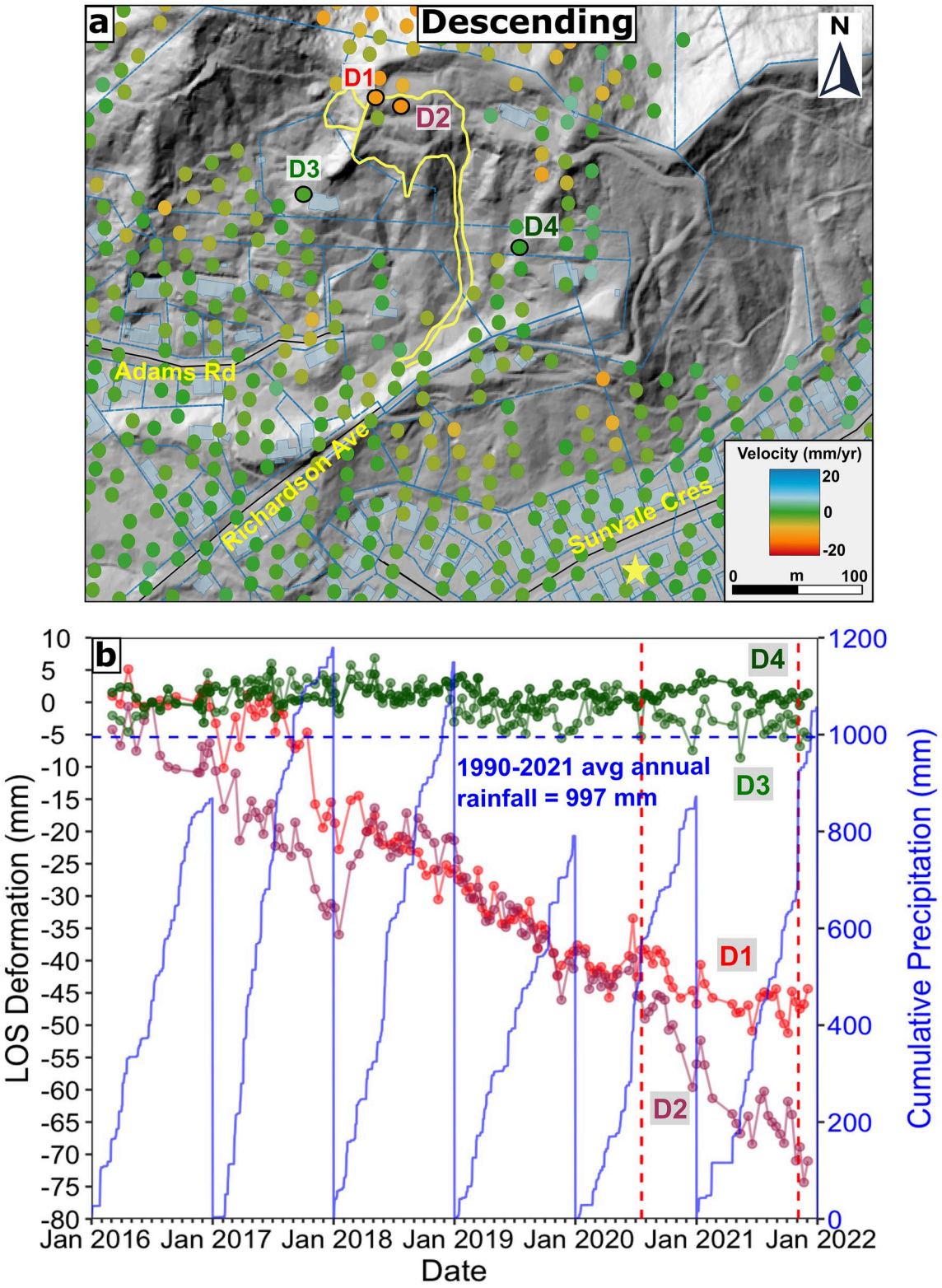


Fig. 8 **a** Descending LOS velocity map overlying the 2019 DEM. The yellow star represents the reference point location. Negative values (red) indicate movement away from the sensor, and positive values are the movement towards the sensor (blue). The labelled points highlighted by black circles represent the data used for the time series plot; **b** compares the LOS deformation of two points from inside the landslide (D1 and D2) and two stable points from outside the deformation area (D3 and D4). The annual cumulative precipitation is also plotted from January 2016 to January 2022 (blue). The horizontal blue dashed line is the average annual cumulative rainfall from 1990 to 2021 (997 mm). The dashed vertical red lines represents the failure events on 20 July 2020 and 4 November 2021

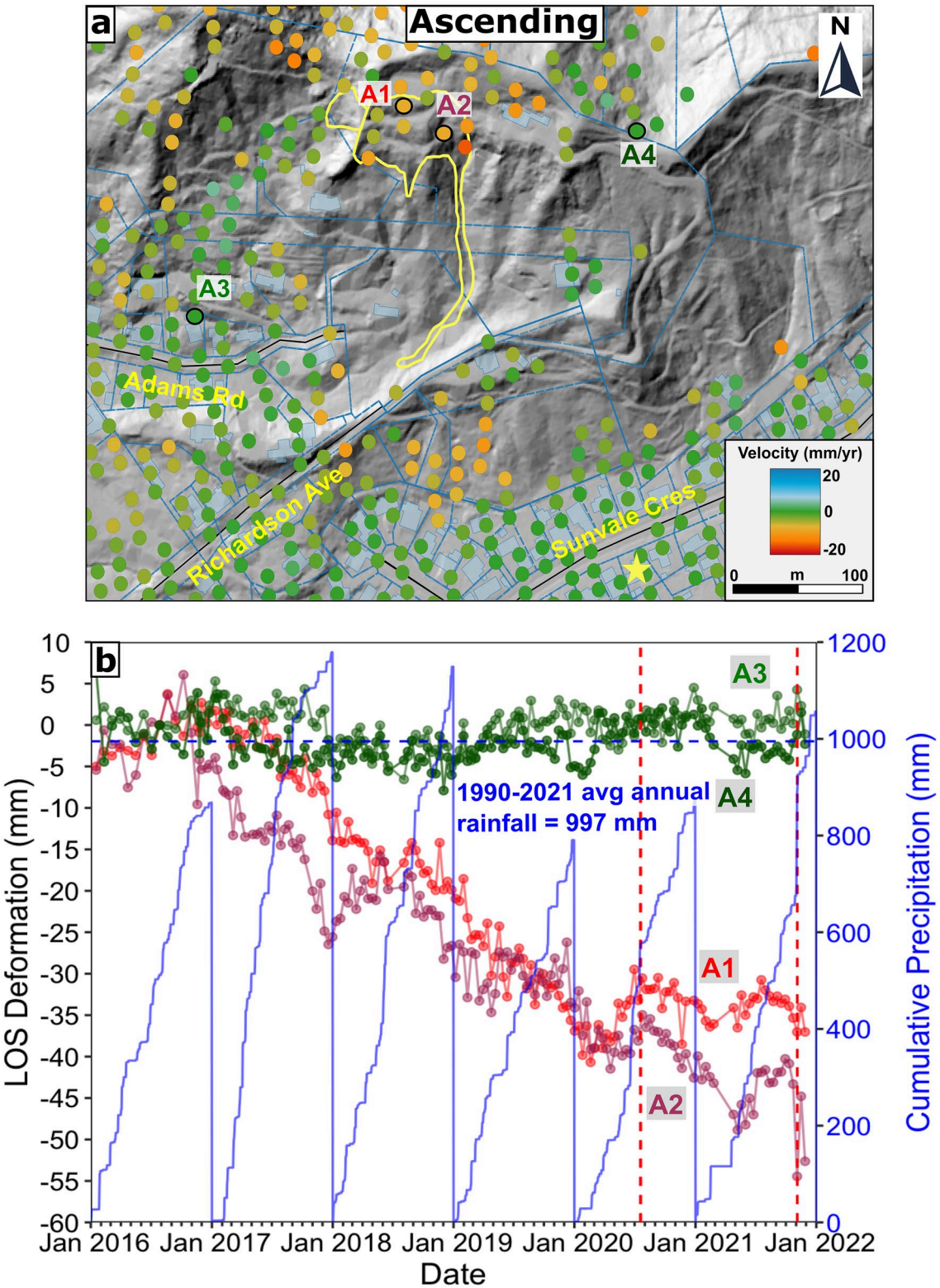


Fig. 9 **a** Ascending LOS velocity map overlying the 2019 DEM. The yellow star represents the reference point location. Negative values (red) indicate movement away from the sensor, and positive values are the movement towards the sensor (blue). The labelled points highlighted by black circles represent the data used for the time series plot; **b** compares the LOS deformation of two points from inside the landslide (A1 and A2) and two stable points from outside the deformation area (A3 and A4). The annual cumulative precipitation is also plotted from January 2016 to January 2022 (blue). The horizontal blue dashed line is the average annual cumulative rainfall from 1990 to 2021 (997 mm). The dashed vertical red line represents the failure event on 20 July 2020 and 4 November 2021

Table 3 Vertical and horizontal velocity components derived from combining the LOS vectors and V_{LOS} of ascending and descending points at the headscarp. Calculations have been rounded to 1 decimal point: V_{VERT}, vertical velocity; V_{EW}, horizontal velocity

Velocity component	D1 and A1	D2 and A1
V_{VERT} (mm/year)	−11.2	−11.9
V_{EW} (mm/year)	−1.5	−2.3

Richardson Avenue landslide is on a south-facing slope, which is perpendicular to the LOS of the satellites. This means the sensors will have a low sensitivity to translational displacements along a north–south direction (Colesanti and Wasowski 2006). The slope must be exactly parallel to the sensor-target direction to obtain the actual deformation vector (Aslan et al. 2020). Nevertheless, in such unfavourable topographic conditions, integration of ascending and descending InSAR measurements can provide useful information on vertical and east–west components of movement, and can resolve the ambiguity in data interpretation (Aslan et al. 2020; Colesanti and Wasowski 2006). Estimating the horizontal and vertical components of the V_{LOS} allowed us to characterise the displacement mechanism of the headscarp. Most of the detected movement was vertical, with maximum values of −11.9 mm/year, while the east–west/translational movement is minor with maximum values of −2.3 mm/year. Failure with a rotational component is known to create vertical movement in the headscarp (e.g. Notti et al. 2014; Wasowski and Pisano 2019), with ~1 m visible at the study site (Fig. 4b, c). Pre-failure, the slope displayed a stepped morphology (Fig. 3a), facilitating detection of slow vertical movement by InSAR. Similar findings were reported by Wasowski and Pisano (2019) and Roberts (2016) when investigating north–south orientated, slow-moving urban landslides. The InSAR results showed a strong vertical component in both studies, related to the rotational motion of the landslide, particularly at the headscarp, and only a small portion of the horizontal motion was detected.

Slope failure processes

The Richardson Avenue landslide is a complex landslide characterised by rotational movement that transitions downslope into a channelised mudflow (e.g. Hungr et al. 2014). It is challenging to isolate the exact conditioning factors that cause landsliding at the site. It is well documented in the region that the interplay of moderate to steep slope angles, rainfall, vegetation cover loss and weak soils all contribute to shallow landsliding (e.g. Basher 2013; Crozier 2010; Dymond et al. 2006; Gao and Maro 2010; Glade 2003; Marden 2012; Phillips et al. 2018). In the Gisborne region, shallow soil failures typically occur within the highly weathered Pleistocene Mangatuna Formation and regolith of the Miocene Tolaga Group mudstone (Mazengarb 1997). At Richardson Avenue, the removal of pine trees from the slope in 2015, particularly where the current headscarp is located, is likely to have disturbed the soils. Lehmann et al. (2019) observed that in New Zealand, where large-scale forest clear-cutting occurred, most landslides happen within the first 3 to 5 years after large-scale deforestation. In this time interval, root systems have not regrown, there is no canopy cover, and so the unvegetated slope becomes more susceptible to elevated groundwater tables during heavy, prolonged rainfall (Marden et al. 2018). Another important factor is slope morphology, with the stepped morphology, steep angle and slope excavations conducive to shallow rotational movement (e.g. Hearn et al. 2011).

The InSAR analysis indicates that continuous slow movement away from the satellites began in March 2017 (Figs. 8 and 9), coinciding with two ex-tropical cyclones crossing Gisborne. Rainfall from both of these weather systems caused extensive shallow landsliding across the North Island (e.g. Palma et al. 2020). The first ex-tropical cyclone (Debbie) crossed Gisborne on 3–6 April 2017, causing 89 mm of rain. Ex-tropical cyclone Cook followed on 11–14 April 2017, causing 64 mm of rain. Although 2017 and 2018 experienced higher than average rainfall (Fig. 8b), no significant slope failure event was recorded during this time. The July 2020 failure occurred after a prolonged dry period, as 2019 and 2020 were years when the annual cumulative rainfall was lower than average. While antecedent rainfall coupled with high 24-hour rainfall thresholds are often important in causing slopes to fail (e.g. Glade 1998), at Richardson Avenue, it is likely that drier conditions promoted shrinking and cracking of vegetation-free smectite-rich soils. A study by Handwerger et al. (2019) showed that slow continuous downslope deformation detected by InSAR occurred between long periods of drought and rainfall on landslides in California, and movement accelerated preceding the failure events. In Gisborne, long-term wet and dry periods are influenced by El Niño Southern Oscillation (ENSO). Indeed, negative ENSO (i.e. El Niño conditions) leads to drier conditions (Cook et al. 2022), with the 2019–2020 El Niño event likely increasing the shrinking and fissuring of the clayey surface soils. The fissuring allows meteoric water to infiltrate deeper and faster than when soils are moist, and any fissures are narrowed (e.g. Palma et al. 2020). It is envisaged in these types of units that water from rainfall events infiltrates down through the soil and into the weathered rock mass, creating temporary "perched" groundwater levels. This may be key to increasing slope deformation at Richardson Avenue, resulting in slopes that are vulnerable to sudden rainfall events. Indeed, rainwater can infiltrate rapidly into the subsurface via fissures, increasing the moisture content in the slope and reducing shear strength. Finally, following the failure in July 2020, while the slope showed signs of stability in the area surrounding the headscarp, retrogressive slumping occurred downslope in areas with existing tension cracks and led to a minor reactivation event triggered by heavy rainfall in November 2021. Site observations accord with the InSAR results from time series for D2 and A2, which show accelerated deformation after July 2020, and a significant increase in deformation immediately prior to the November 2021 reactivation. Other studies using spaceborne InSAR to measure deformation on landslides have also reported continued deformation post-failure (Confuorto et al. 2017; Roberts et al. 2019), which highlights the ability of InSAR to monitor the evolution of a slope and give valuable insight on slope movement pre- and post-failure.

Conclusions

We have provided a case study investigation of an urban landslide at a residential site in suburban Gisborne, New Zealand. The soft, sensitive smectite-rich surface materials are vulnerable to changes in moisture content, particularly following the removal of vegetation. The Richardson Avenue landslide is "complex", with an upper area of slumping below the ridgeline where the house is sited, transitioning downslope into a zone of channelised flows, constrained within a

gulley. Recent surface deformation was observed using InSAR, and the data set revealed detected slow deformation on the slope in the vertical direction, related to the characteristic rotational slumping exhibited by the upper section of the landslide in July 2020. The longer-term deformation time series (2016–2021) indicates that the large-scale failure at the site occurred only after vegetation stripping in 2015, which left the soils vulnerable to significant rainfall during the passage of two ex-tropical cyclones that followed in 2017. Prior to the November 2021 reactivation event, deformation rates were observed to accelerate on the lower part of the rotational segment, relative to the upper segment, showing the InSAR methodology can resolve differential movement in a complex flow field. Nevertheless, the south-facing slope geometry of the Richardson Avenue landslide is somewhat unfavourable for Sentinel-1 InSAR, because it is perpendicular to the LOS. This alignment makes InSAR analysis challenging particularly for detecting translational movement downslope. This highlights the site-specific complexities in utilising InSAR for monitoring some landslide sites. The future of the Richardson Avenue site is likely one of slow continuous deformation, followed by velocity increases following rainfall events. In these sensitive soils, the timing and rate of velocity increases will relate to the interplay of antecedent soil moisture and high intensity rainfall from the passage of extra-tropical cyclones.

Acknowledgements

Jill Wall is thanked for allowing access and information about the landslide. Gisborne District Council is thanked for provision of the LiDAR data. University of Auckland technician David Wackrow provided laboratory assistance, while the National Institute of Water and Atmospheric Research (NIWA) provided climate station data via their Cliflo database.

Funding

Open Access funding enabled and organized by CAUL and its Member Institutions. This research is funded by the Earthquake Commission (EQC) via grant number 18/U770 and 1965/20799, which funded Matthew Cook's PhD scholarship.

Data Availability

The data that support the findings of this study are available from the Gisborne District Council but restrictions apply to the availability of these data, which were used under licence for the current study, and so are not publicly available. Data are however available from the authors upon reasonable request and with permission of the Gisborne District Council.

Declarations

Competing interests The authors declare no competing interests.

Open Access This article is licensed under a Creative Commons Attribution 4.0 International License, which permits use, sharing, adaptation, distribution and reproduction in any medium or format, as long as you give appropriate credit to the original author(s) and the source, provide a link to the Creative Commons licence, and indicate if changes were made. The images or other third party material in this article are included in the article's Creative Commons licence, unless indicated otherwise in a credit line to the material. If material is not included in the article's Creative Commons licence and your intended use is not permitted by statutory regulation or exceeds the permitted use, you will need to obtain permission directly from the copyright holder. To view a copy of this licence, visit http://creativecommons.org/licenses/by/4.0/.

References

Aslan G, Foumelis M, Raucoules D, de Michele M, Bernardie S, Cakir Z (2020) Landslide mapping and monitoring using persistent scatterer interferometry (PSI) technique in the French Alps. Remote Sens 12(8):1305. https://doi.org/10.3390/rs12081305

Asuri S, Keshavamurthy P (2016) Expansive soil characterisation: an appraisal. INAE Lett 1(1):29–33. https://doi.org/10.1007/s41403-016-0001-9

Basher LR (2013) Erosion processes and their control in New Zealand. In: Dymond JR (ed) Ecosystem services in New Zealand – conditions and trends. Manaaki Whenua Press, Lincoln, New Zealand, pp 363–374

Béjar-Pizarro M, Notti D, Mateos RM, Ezquerro P, Centolanza G, Herrera G, Bru G, Sanabria M, Solari L, Duro J, Fernández J (2017) Mapping vulnerable urban areas affected by slow-moving landslides using Sentinel-1 InSAR data. Remote Sens 9(9):876. https://doi.org/10.3390/rs9090876

Bekaert DP, Handwerger AL, Agram P, Kirschbaum DB (2020) InSAR-based detection method for mapping and monitoring slow-moving landslides in remote regions with steep and mountainous terrain: an application to Nepal. Remote Sens of Environ 249:111983. https://doi.org/10.1016/j.rse.2020.111983

Berardino P, Fornaro G, Lanari R, Sansosti E (2002) A new algorithm for surface deformation monitoring based on small baseline differential SAR interferograms. IEEE Transactions on Geoscience and Remote Sens 40(11):2375–2383. https://doi.org/10.1109/tgrs.2002.803792

BSI (1998) BS 1377–2. Methods of test for soils for civil engineering purposes – part 2: classification tests. British Standards Institution, London, United Kingdom

Burns D, Farqhuar G, Mills M, Williams A (2005) Field description of soil and rock. NZ Geotech Society. Available at: https://www.nzgs.org/library/field-description-of-soil-and-rock/

Chaney R, Demars K, Gabr M, Coonse J, Lambe P (2001) A potential model for compaction evaluation of piedmont soils using dynamic cone penetrometer (DCP). Geotech Test J 24(3):308. https://doi.org/10.1520/gtj11349j

Claessens L, Schoorl J, Veldkamp A (2007) Modelling the location of shallow landslides and their effects on landscape dynamics in large watersheds: an application for Northern New Zealand. Geomorphol 87(1–2):16–27. https://doi.org/10.1016/j.geomorph.2006.06.039

Colesanti C, Wasowski J (2006) Investigating landslides with space-borne Synthetic Aperture Radar (SAR) interferometry. Eng Geol 88(3–4):173–199. https://doi.org/10.1016/j.enggeo.2006.09.013

Confuorto P, di Martire D, Centolanza G, Iglesias R, Mallorqui JJ, Novellino A, Plank S, Ramondini M, Thuro K, Calcaterra D (2017) Post-failure evolution analysis of a rainfall-triggered landslide by multi-temporal interferometry SAR approaches integrated with geotechnical analysis. Remote Sens of Environ 188:51–72. https://doi.org/10.1016/j.rse.2016.11.002

Cook ME, Brook MS, Tunnicliffe J, Cave M, Gulick NP (2022) Preliminary investigation of emerging suburban landsliding in Gisborne, New Zealand. Q J Eng Geol Hydrogeol qjegh2021–087. https://doi.org/10.1144/qjegh2021-087

Crozier M (2010) Landslide geomorphology: an argument for recognition, with examples from New Zealand. Geomorphol 120(1–2):3–15. https://doi.org/10.1016/j.geomorph.2009.09.010

Davies N, Cave M (2017) Slope instability Wallis Road. Initial Technical Report. Gisborne, New Zealand

Del Soldato M, Solari L, Poggi F, Raspini F, Tomás R, Fanti R, Casagli N (2019) Landslide-induced damage probability estimation coupling InSAR and

field survey data by fragility curves. Remote Sens 11(12):1486. https://doi.org/10.3390/rs11121486
Dymond JR, Ausseil AG, Shepherd JD, Buettner L (2006) Validation of a region-wide model of landslide susceptibility in the Manawatu-Wanganui region of New Zealand. Geomorphol 74(1–4):70–79. https://doi.org/10.1016/j.geomorph.2005.08.005
Ferretti A, Colombo D, Fumagalli A, Novali F, Rucci A (2015) InSAR data for monitoring land subsidence: time to think big. Proceedings of the International Association of Hydrol Sci 372:331–334. https://doi.org/10.5194/piahs-372-331-2015
Fityus S, Buzzi O (2009) The place of expansive clays in the framework of unsaturated soil mechanics. Appl Clay Sci 43(2):150–155. https://doi.org/10.1016/j.clay.2008.08.005
Gao J, Maro J (2010) Topographic controls on evolution of shallow landslides in pastoral Wairarapa, New Zealand, 1979–2003. Geomorphol 114(3):373–381. https://doi.org/10.1016/j.geomorph.2009.08.002
Galli M, Ardizzone F, Cardinali M, Guzzetti F, Reichenbach P (2008) Comparing Landslide Inventory Maps Geomorphol 94(3–4):268–289. https://doi.org/10.1016/j.geomorph.2006.09.023
Glade T (1998) Establishing the frequency and magnitude of landslide-triggering rainstorm events in New Zealand. Environ Geol 35(2–3):160–174. https://doi.org/10.1007/s002540050302
Glade T (2003) Landslide occurrence as a response to land use change: a review of evidence from New Zealand. CATENA 51(3–4):297–314. https://doi.org/10.1016/s0341-8162(02)00170-4
Grace ES (2014) Gisborne District Risk Assessment. GNS Science Consultancy Report, 2014/279
Handwerger AL, Huang MH, Fielding EJ, Booth AM, Bürgmann R (2019) A shift from drought to extreme rainfall drives a stable landslide to catastrophic failure. Sci Rep 9(1). https://doi.org/10.1038/s41598-018-38300-0
Hearn GJ, Hunt T, D'Agostino S (2011) C3 soil slope stabilization. Geological Society, London, Eng Geol Spec Publ 24(1):165–188. https://doi.org/10.1144/egsp24.12
Hungr O, Leroueil S, Picarelli L (2014) The Varnes classification of landslide types, an update. Landslides 11(2):167–194. https://doi.org/10.1007/s10346-013-0436-y
Intrieri E, Raspini F, Fumagalli A, Lu P, del Conte S, Farina P, Allievi J, Ferretti A, Casagli N (2017) The Maoxian landslide as seen from space: detecting precursors of failure with Sentinel-1 data. Landslides 15(1):123–133. https://doi.org/10.1007/s10346-017-0915-7
Isya NH, Niemeier W, Gerke M (2019) 3D Estimation of slow ground motion using InSAR and the slope aspect assumption, a case study: the Puncak Pass landslide, Indonesia. ISPRS Annals of Photogrammetry. Remote Sens Spat Infor Sci IV-2/W5:623–630. https://doi.org/10.5194/isprs-annals-iv-2-w5-623-2019
Jol HM (2008) Ground penetrating radar: theory and applications. Elsevier, Amsterdam
Kim J, Jeong S, Park S, Sharma J (2004) Influence of rainfall-induced wetting on the stability of slopes in weathered soils. Eng Geol 75(3–4):251–262. https://doi.org/10.1016/j.enggeo.2004.06.017
Lehmann P, Ruette J, Or D (2019) Deforestation effects on rainfall-induced shallow landslides: remote sensing and physically-based modelling. Water Resour Res 55(11):9962–9976. https://doi.org/10.1029/2019wr025233
Marden M (2012) Effectiveness of reforestation in erosion mitigation and implications for future sediment yields, East Coast catchments. New Zealand: A Review NZ Geogr 68(1):24–35. https://doi.org/10.1111/j.1745-7939.2012.01218.x
Marden M, Fuller IC, Herzig A, Betts HD (2018) Badass gullies: Fluvio-mass-movement gully complexes in New Zealand's East Coast region, and potential for remediation. Geomorphol 307:12–23. https://doi.org/10.1016/j.geomorph.2017.11.012
Mazengarb C (1997) Slope instability and mud volcano hazard assessment, Gisborne District Council. Institute of Geological and Nuclear Sciences client report. 44692d. 13A
Meunier A (2006) Why are clay minerals small? Clay Miner 41(2):551–566. https://doi.org/10.1180/0009855064120205
Minder JR, Roe GH, Montgomery DR (2009) Spatial patterns of rainfall and shallow landslide susceptibility. Water Resour Res 45(4). https://doi.org/10.1029/2008wr007027
Notti D, Herrera G, Bianchini S, Meisina C, García-Davalillo JC, Zucca F (2014) A methodology for improving landslide PSI data analysis. Int J of Remote Sens 35(6):2186–2214. https://doi.org/10.1080/01431161.2014.889864
Palma A, Garrill R, Brook MS, Richards N, Tunnicliffe J (2020) Reactivation of coastal landsliding at Sunkist Bay, Auckland, following ex-Tropical Cyclone Debbie, 5 April 2017. Landslides 17(11):2659–2669. https://doi.org/10.1007/s10346-020-01474-8
Phillips C, Marden M, Basher LR (2018) Geomorphology and forest management in New Zealand's erodible steeplands: an overview. Geomorphol 307:107–121. https://doi.org/10.1016/j.geomorph.2017.07.031
Roberts NJ (2016) Late Cenozoic geology of La Paz, Bolivia, and its relation to landslide activity. Doctoral dissertation, Science: Simon Fraser University, Department of Earth Sciences. Available at: https://summit.sfu.ca/item/16449
Roberts NJ, Rabus BT, Clague JJ, Hermanns RL, Guzmán MA, Minaya E (2019) Changes in ground deformation prior to and following a large urban landslide in La Paz, Bolivia, revealed by advanced InSAR. Nat Hazards and Earth Syst Sci 19(3):679–696. https://doi.org/10.5194/nhess-19-679-2019
Rosen PA, Gurrola E, Sacco GF, Zebker H (2012) The InSAR scientific computing environment. In EUSAR 2012; 9th European Conference on Synthetic Aperture Radar 730–733
Rosser B, Dellow S, Haubrock S, Glassey P (2017) New Zealand's National Landslide Database Landslides 14(6):1949–1959. https://doi.org/10.1007/s10346-017-0843-6
Skempton AW, Northey RD (1952) The Sensitivity of Clays Géotechnique 3(1):30–53. https://doi.org/10.1680/geot.1952.3.1.30
Tang H, Li C, Hu X, Su A, Wang L, Wu Y, Criss R, Xiong C, Li Y (2014) Evolution characteristics of the Huangtupo landslide based on in situ tunneling and monitoring. Landslides 12(3):511–521. https://doi.org/10.1007/s10346-014-0500-2
Torrance JK (2014) Chemistry, sensitivity and quick-clay landslide amelioration. In: Landslides in Sensitive Clays. Springer, Dordrecht. 15–24. https://doi.org/10.1007/978-94-007-7079-9_2
Uhlemann S, Smith A, Chambers J, Dixon N, Dijkstra T, Haslam E, Meldrum P, Merritt A, Gunn D, Mackay J (2016) Assessment of ground-based monitoring techniques applied to landslide investigations. Geomorphol 253:438–451. https://doi.org/10.1016/j.geomorph.2015.10.027
Wasowski J, Bovenga F (2014) Investigating landslides and unstable slopes with satellite Multi Temporal Interferometry: current issues and future perspectives. Eng Geol 174:103–138. https://doi.org/10.1016/j.enggeo.2014.03.003
Wasowski J, Pisano L (2019) Long-term InSAR, borehole inclinometer, and rainfall records provide insight into the mechanism and activity patterns of an extremely slow urbanized landslide. Landslides 17(2):445–457. https://doi.org/10.1007/s10346-019-01276-7
Wesley LD (2010) Geotechnical Engineering in Residual Soils. John Wiley & Sons
Yunjun Z, Fattahi H, Amelung F (2019) Small baseline InSAR time series analysis: unwrapping error correction and noise reduction. Computer Geosci 133:104331. https://doi.org/10.1016/j.cageo.2019.104331

Matthew E. Cook (✉) · **Martin S. Brook** · **Jon F. Tunnicliffe** · **David J. Alama**
School of Environment, The University of Auckland, Auckland 1010, New Zealand
Email: mcoo951@aucklanduni.ac.nz

Ian J. Hamling
GNS Science, Lower Hutt, Wellington, New Zealand

Murry Cave
Gisborne District Council, Gisborne 4010, New Zealand

Rachel Holley
CGG Satellite Mapping, Crockham Park, Edenbridge TN8 6SR, UK